Morphology and seasonal variations of global auroral proton precipitation observed by IMAGE-FUV

Valérie Coumans, Jean-Claude Gérard, and Benoît Hubert
Laboratoire de Physique Atmosphérique et Planétaire, Université de Liège, Liège, Belgium

Stephen B. Mende
Space Science Laboratory, University of California, Berkeley, California, USA

Stanley W. H. Cowley
Department of Physics and Astronomy, University of Leicester, Leicester, UK

Received 5 December 2003; revised 9 July 2004; accepted 13 October 2004; published 10 December 2004.

[1] Observations with the FUV imagers on board the IMAGE satellite have been used to map the auroral electron and proton energy fluxes during the summer and winter solstices of 2000, in order to construct a statistical view of the global auroral proton precipitation. The distribution for electrons compare well both in morphology and in magnitude with those obtained previously with the Polar-UVI instruments and with an empirical auroral precipitation model based on DMSP data. The proton morphology also closely resembles the statistical ion oval derived from DMSP data, showing a "C-shaped" morphology with a minimum located in the morning sector. The precipitation proton auroral power is on the order of 2.2 GW for an average Kp value of 2, also in close agreement with the values of the DMSP empirical model. The FUV data also reveal the presence of seasonal effects in the proton precipitation. Specifically, the latitudinal width of the proton oval is larger in summer than in winter so that the globally precipitated proton power is 1.5 times higher in summer than in winter. The occurrence probability of intense proton auroras (with energy flux >0.5 mW m^{-2}) is also shown to be nearly three times higher in summer than in winter. This seasonal effect in the proton precipitation contrasts with those observed for electrons, where intense electron events occur more often in winter than in summer. We discuss a mechanism that may account for these results based on the presence of field-aligned potential drops which accelerate auroral electrons downward in regions of upward directed field-aligned current, while suppressing the precipitating magnetospheric proton flux. The presence of such field-aligned potentials is dependent on the differing solar illumination in winter and summer. *INDEX TERMS:* 2716 Magnetospheric Physics: Energetic particles, precipitating; 2712 Magnetospheric Physics: Electric fields (2411); 2704 Magnetospheric Physics: Auroral phenomena (2407); 2431 Ionosphere: Ionosphere/magnetosphere interactions (2736); 2451 Ionosphere: Particle acceleration; *KEYWORDS:* proton aurora, global morphology, seasonality, statistical energy flux

Citation: Coumans, V., J.-C. Gérard, B. Hubert, S. B. Mende, and S. W. H. Cowley (2004), Morphology and seasonal variations of global auroral proton precipitation observed by IMAGE-FUV, *J. Geophys. Res.*, *109*, A12205, doi:10.1029/2003JA010348.

1. Introduction

[2] The proton auroral region is located at the feet of magnetic field lines where protons precipitate downward into the atmosphere and interact with neutral atmospheric constituents to produce auroral hydrogen emission. The poleward limit of this region corresponds to the boundary between open and closed magnetic field lines. The equatorward limit is generally coincident with the isotropic boundary, which is the boundary between regions of adiabatic and stochastic proton motion in the equatorial tail current sheet [*Sergeev et al.*, 1983]. The field lines closer to the Earth are dipole-like, where trapped protons experience little pitch angle scattering or other processes that populate the loss cone under quiet conditions. Protons in this region are stably trapped. *Mende et al.* [2002] have discussed four processes that may produce significant precipitation. First, proton aurora can be produced by precipitation from an isotropic proton population injected into a region of closed field lines, for example by dayside reconnection or nightside substorm processes. Second, under some active circumstances, significant precipitation from a stably trapped population can also be produced by pitch angle diffusion due to particle interactions with electric fields (dc or wave). The loss cone is then populated, and trapped particles will

0148-0227/04/2003JA010348$09.00

move down into the atmosphere. Third, precipitation can also be produced when a magnetic reconfiguration compresses the region occupied by the particles, for example, following a solar wind-induced compression of the magnetosphere. Fourth, proton precipitation also occurs when particles are scattered in a stretched field line configuration, such that the proton motion is no longer adiabatic. Some of these processes occur only during substorms, but because of the magnetic configuration of the magnetosphere, weak precipitation at latitudes exceeding the isotropic boundary takes place continuously.

[3] To date, the global morphology of auroral precipitation has been analyzed using two different methods. First, a statistical approach was used by *Hardy et al.* [1985, 1989], who employed in situ data obtained from ~27,000 polar passes by DMSP spacecraft. Statistical maps of the mean particle energy, number flux, and energy flux were provided for electrons and protons for seven different magnetic activity levels measured by the Kp index. It was already known prior to these studies that both proton and electron precipitation occur within annular regions which are roughly colocated. Ground-based measurements had also shown that the auroral proton pattern intensifies and moves equatorward with increasing geomagnetic and substorm activity [*Vallance Jones et al.*, 1982, and references therein]. *Hardy et al.* [1989] emphasized the fact that a minimum in the ion energy flux occurs in the prenoon sector, while the maximum value is observed premidnight at all levels of activity. Comparison with results for electrons of *Hardy et al.* [1985] also showed that the peak ion energy flux is located equatorward of the peak electron energy flux in the dusk sector. The second approach was initiated by the Dynamics Explorer 1 mission [*Frank and Craven*, 1988], which provided global FUV images of the auroral region. Similar global images from the Polar UVI instrument have been analyzed by *Liou et al.* [2001] to determine the statistical characteristics of global auroral precipitation and its seasonal variations. However, no detailed comparisons have yet been made with the statistical studies based on DMSP data. In addition, no study has been made of proton precipitation using global FUV images, since the above imagers could not discriminate between proton and electron precipitation. A new era started with the launch of the IMAGE satellite in March 2000, which carries a multispectral FUV imaging system including the SI12 camera sensitive to Doppler-shifted Lyman-α emission providing snapshots of the global proton precipitation. We emphasize that statistical maps obtained from in situ measurements and from IMAGE-FUV global images are based on two very different approaches. Particles studies build statistical maps from a large set of measurements made along the satellite track, and since satellite orbits drift slowly in local time it is often difficult to decouple local time and seasonal dependences. By contrast, the IMAGE-FUV study discussed here is based on global images which cover the entire auroral oval simultaneously. Therefore the results of these two methods do not necessarily lead to the same global picture of the auroral morphology.

[4] Seasonal effects in the auroral electron precipitation have been observed in data from both the DMSP satellites [*Newell et al.*, 1996a] and the Polar images [*Liou et al.*, 2001]. *Liou et al.* [2001] found that the dayside auroral power is enhanced in the summer, while nightside emission is suppressed. They found that the summer nightside suppression is due to a decrease in the average electron energies, while the summer dayside enhancement is due to an increase in the electron number flux. *Newell et al.* [1996a] showed that intense electron events are suppressed under sunlit conditions. Such events, with energy fluxes higher than 5 mW m^{-2}, were found to be associated with discrete auroral arcs, based on an examination of electron energy spectra. The ''sunlight'' effect is also clearly related to the seasonal effect, since the time of year determines the amount of sunlight present. Indeed, *Newell et al.* [2001] found that the same 3:1 ratio in the frequency of occurrence of intense aurora was obtained whether the data were divided by season into winter and summer solstice conditions or by solar zenith angle into cases with angles >110° and <85°. These observations were explained in terms of an ionospheric conductivity feedback mechanism. In this conceptual model the precipitating auroral electrons create an enhanced ionospheric Pedersen conductivity, the response to which depends on whether the background ionospheric conductivity is high or low. If the background ionospheric conductivity is high, a polarization electric field is produced, which reduces the convection electric field and limits the growth of the current. On the other hand, if the background ionospheric conductivity is low, the enhanced ionospheric Pedersen conductivity induces an enhanced Pedersen current. Through ionosphere-magnetosphere coupling, the enhanced currents create a field aligned potential drop which accelerates the auroral electrons downward, which ultimately creates the auroral arcs. Owing to EUV solar radiation the background ionospheric conductivity on the dayside is higher than on the nightside, thus explaining the suppression of nightside electron auroral arcs during the summer. In this picture the seasonality is due to the seasonal variation of the ionospheric illumination by the Sun.

[5] Here we first describe a statistical study based on IMAGE-FUV observations that provides maps of the auroral particle energy flux, which can be compared with related results obtained from in situ measurements [*Hardy et al.*, 1985, 1989]. Results obtained for electron precipitation are compared with those from earlier studies. The electron energy flux maps are used to determine the averaged morphology of the electron precipitation separately for winter and summer, from which the probability of occurrence of intense electron aurora is determined. The same procedure is applied for proton precipitation. Second, we examine the statistical proton energy flux maps to determine possible seasonal dependences. The results for protons are compared to those for the electrons.

2. Data Analysis

[6] The analysis presented here is based on imaging data from the IMAGE satellite, which has an eccentric orbit with a ~7 Earth radii apogee and a 1000-km perigee. The IMAGE FUV imaging system provides a snapshot of the global northern auroral region every 2 min. The Wideband Imaging Camera (WIC) is mostly sensitive to the LBH bands of molecular nitrogen and the 149.3 nm NI line. The SI12 Spectrographic Imager images the Doppler-shifted Lyman-α emission (121.8 nm) produced by auroral protons,

while the SI13 camera isolates the OI 135.6 nm emission [*Mende et al.*, 2000] with some contributions of the N_2 LBH bands. The WIC and SI13 images are contaminated by a dayglow on the dayside, which is subtracted using the method described by *Hubert et al.* [2002]. The SI12 images also contain a weak background contribution that has also been removed from each individual image. This background signal is mainly due to the geocoronal H Lyman-α emission at 121.56 nm and depends on the illumination and view angles. A very small contribution also originates from the N 120 nm emission and from some weak N_2 LBH emission lines. Moreover, dark counts in the detector are also present over the SI12 images. This background contribution is small and may be efficiently removed by a mathematical method, consisting in a polynomial least squares regression. The regression is applied to each SI12 image over the region void of auroral emission and the function so determined is then subtracted over the full observed disk.

[7] For this study we selected a period of 12 days in summer 2000 (14–17 June plus 21–28 June) and 15 days in winter 2000 (15–29 December). This database includes 10,602 WIC images and the same number of SI12 and SI13 images, corresponding to a total of 6.95×10^8 WIC pixels and 1.73×10^8 SI12 and SI13 pixels. Thus although the time period is restricted to intervals close to the solstices, the statistical study is based on a large number of individual FUV samples in the Northern Hemisphere. The two time intervals selected for this study correspond to very similar values of the mean solar flux so that the study is not biased by the level of solar activity. The mean $F_{10.7}$ index was 184 in the summer interval and 191 during the winter interval. The corresponding mean Kp index was 2.6 in summer, compared with 1.5 in the winter. Similarly, the mean hemispheric power derived from NOAA POES satellite measurements [*Lummerzheim et al.*, 1997] was 25.3 GW in the summer and 20.2 GW in winter. Both indices thus show that the activity level was quite close during the two intervals, though slightly higher in the summer interval than in the winter interval.

[8] For each set of three simultaneous FUV images, global maps of the electron average energy, the electron energy flux, and the proton energy flux were calculated. The method and associated uncertainties were described previously by *Hubert et al.* [2002] and *Meurant et al.* [2003]. The determination of the electron mean energy is based on the ratio between simultaneous WIC and SI13 images [*Meurant et al.*, 2003; *Coumans et al.*, 2004]. The precipitating electron energy flux is calculated from the WIC images using the estimated mean energy and the WIC efficiency function. The method used to obtain the proton energy flux [*Gérard et al.*, 2001] is also based on the SI12 efficiency function. An assumption is required concerning the proton energy, since it cannot be determined from the observations. The *Hardy et al.* [1989] empirical mean energy model, which was constructed from in situ DMSP measurements, was therefore used for this purpose. For each FUV pixel the mean proton energy was evaluated from the model, using its geomagnetic location and the concurrent Kp value. The proton energy fluxes are then obtained from the SI12 count rate using the relationship between the SI12 signal and the NOAA in situ measurements of proton precipitation [*Coumans et al.*, 2002]. The proton flux so derived is also used to remove the proton contribution from the WIC and the SI13 images. This method was validated by comparisons with in situ measurements of the auroral particle energy flux obtained from the FAST [*Frey et al.*, 2001; *Bisikalo et al.*, 2003], NOAA [*Hubert et al.*, 2002; *Coumans et al.*, 2002; *Meurant et al.*, 2003], and DMSP [*Bisikalo et al.*, 2003; *Coumans et al.*, 2004] satellites.

[9] The determination of the statistical particle energy flux patterns requires the FUV observations to be mapped into geomagnetic coordinates. The mapping technique is based on the classical Delaunay triangulation method, constructed in a manner to avoid information loss. The magnetic latitude system employed is the modified apex coordinate system defined by *Richmond* [1995]. The statistical models derived by *Hardy et al.* [1985, 1989], on the other hand, are defined in corrected geomagnetic coordinates. However, *Richmond* [1995] emphasized the fact that magnetic apex coordinates are very similar to corrected geomagnetic coordinates for magnetic field lines intersecting the ionosphere at high latitudes. Specifically, *Gasda and Richmond* [1998] noticed that at auroral latitude ($\sim$68° MLAT), the maximum difference between the apex magnetic latitude at 110 km and corrected geomagnetic latitude at ground level is 0.17°, which is smaller than the IMAGE-FUV resolution. Therefore in this paper we thus use the term "magnetic latitude" to mean either apex or corrected magnetic latitude.

3. Electron Fluxes and Probability of Intense Electron Aurora

[10] The averaged precipitating electron energy flux was calculated for the summer and winter intervals given above using the method outlined. As mentioned before, the dayside sector of the WIC and SI13 images is contaminated by dayglow, mainly in the summer. The dayglow subtraction method in these imagers, however, is not sufficiently accurate for our purposes so that reliable statistics on summer electron precipitation cannot be obtained. At winter solstice, a large part of the Northern Hemisphere is in darkness, thus allowing electron precipitation parameters to be derived free of dayglow contamination. Figure 1a thus shows results for the nightside winter data only, where the region around noon up to 77° MLAT has been omitted, since contamination is still present following background subtraction. The maximum value of the mean winter electron energy flux pattern is located in the premidnight sector, between 2100 and 2400 MLT, at around 70° MLAT, and reaches 1.6 mW m^{-2}. The auroral oval is seen to extend between 65° and 75° MLAT in the premidnight sector, between 60° and 75° MLAT in the postmidnight sector, and between 65° and 80° MLAT in the morning sector. The energy flux decreases with decreasing MLTs in the dusk sector and reaches a value below 0.5 mW m^{-2} in the afternoon sector around $\sim$1730 and 73° MLAT.

[11] We now compare our winter electron energy flux map with the *Hardy et al.* [1985] statistical model, which was derived from DMSP measurements and binned by Kp level. Figure 1b shows the *Hardy et al.* [1985] energy flux map using a weighted Kp index evaluated for our winter 2000 interval. A weighting factor was calculated for each Kp value from the ratio of the number of images obtained

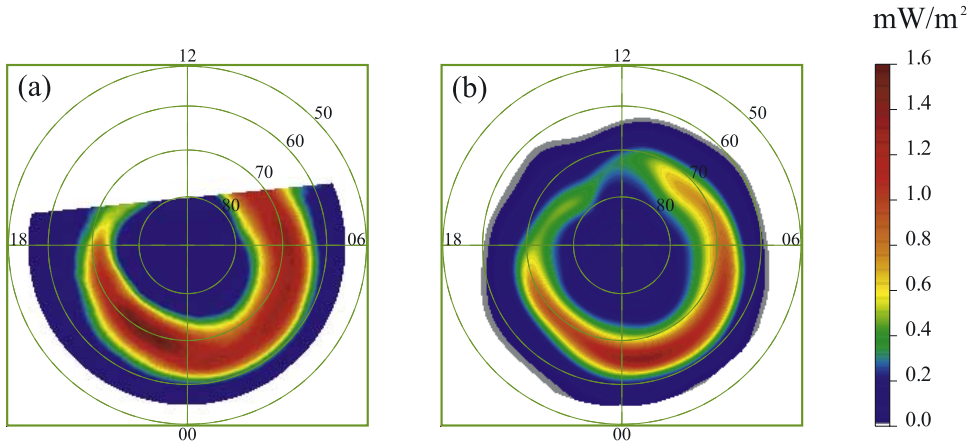

Figure 1. Maps of the mean electron energy flux (a) from our statistical study using IMAGE-FUV data in winter 2000 for all Kp values and (b) from the *Hardy et al.* [1985] model with a weighted Kp index but without seasonal discrimination.

for that Kp value and the total number of images obtained during the interval. Each DMSP precipitation pattern was then multiplied by the associated weighting factor and added together to obtain Figure 1b. It can be seen that the shape of the pattern and the range of electron energy flux values are quite similar to those found here, in the region without dayglow contamination. The pattern is characterized by a C-shaped morphology with a minimum in the afternoon sector. The maximum is located in the postmidnight sector and reaches $\sim$1.4 mW m^{-2}. A difference is that the precipitation region determined from the in situ particle data is somewhat narrower than the FUV oval. This is possibly a seasonal difference and/or due to the difference of the spatial resolution of the DMSP and IMAGE instruments. It should also be borne in mind that the *Hardy et al.* [1985] statistical model does not differentiate between seasons, while the IMAGE-FUV map in Figure 1a was derived specifically from winter observations. Overall, however, the general agreement between these two sets of results is quite satisfactory, considering the different resolution and approach used to build the statistical SI12 and DMSP global map.

[12] Related results were also obtained by *Liou et al.* [2001] using Polar-UVI measurements. The averaged precipitating electron energy flux derived for winter conditions from Polar-UVI images also exhibits a C-shaped pattern, with a minimum in the afternoon and a maximum premidnight, similar to Figure 1a. The magnitude of the premidnight maximum was 25% higher than in Figure 1a, reaching 2 mW m^{-2}. This small difference is within the uncertainties in the calibration of the instruments. In addition, part of the difference may also stem from the different level of solar activity in the two databases. We also note that the Polar UVI images include a contribution due to proton precipitation that could not be removed, which also plays a role in the energy flux difference noted above.

[13] In Figure 2a we also show the occurrence probability distribution for observing intense electron aurora in the IMAGE data. For each pixel we have calculated the ratio between the number of cases where the energy flux is higher than 5 mW m^{-2} and the total number of cases. The region between 0730 and 1630 MLT has been masked out to avoid dayglow contamination. Within the region shown, the probability pattern is C-shaped, with a maximum of about

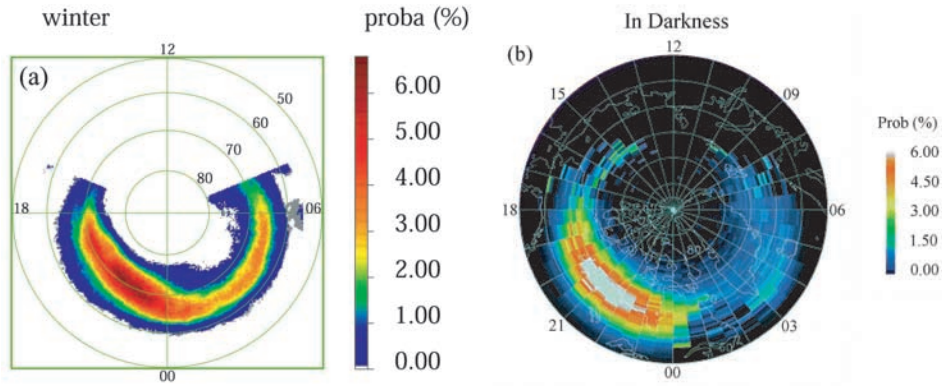

Figure 2. (a) Probability of occurrence of intense electron aurora in winter 2000 as a function of magnetic latitude and local time determined from IMAGE-FUV observations and (b) related DMSP observations from *Newell et al.* [1996a].

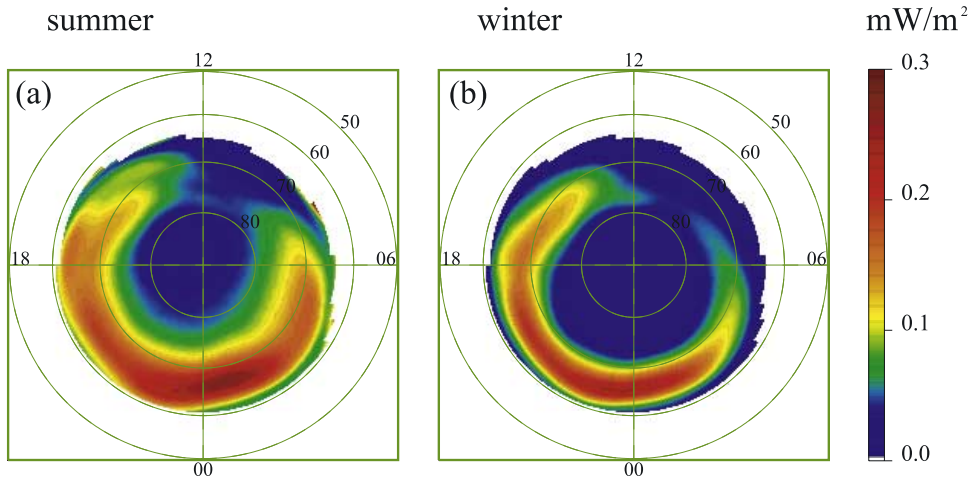

Figure 3. Averaged energy flux maps for protons evaluated from IMAGE-FUV observations for (a) our summer and (b) our winter intervals, displayed in geomagnetic coordinates.

7% in the 2100–2400 MLT sector at around 70° MLAT. The probability decreases on sectors going to the dayside, around 1700 MLT and 70° MLAT and around 0430 MLT and 68° MLAT. In the postmidnight sector between 0230 and 0600 MLT and 60°–70° MLAT the probability reaches ~3.5%. At around 0200 MLT and 65° MLAT, however, the probability locally drops to 3%. In Figure 2b we show related results obtained by *Newell et al.* [1996a] from DMSP data, specifically the probability of observing accelerated electron distributions associated with the discrete aurora. The comparison shows very good agreement with our results, both in morphology and in magnitude. The maximum probability is around 6% in the 2000–2300 MLT sector, while the minimum probability is located near noon, with a secondary local minimum in the postmidnight sector. We note, however, that the peak value in the postmidnight sector between 0230 and 0600 MLT is 1.5% in the DMSP study, which is lower than that in Figure 2a. This difference may be related to the fact that the DMSP study used 9 years of measurements, almost encompassing a complete solar cycle, while we have only included FUV observations obtained in a period close to solar maximum. In addition, the DMSP methodology used to obtain this map also employed additional criteria based on the evolution of the electron energy spectra along the orbit.

[14] Overall, we conclude from the results shown in this section that our winter electron statistical precipitation pattern is in adequate agreement with earlier in situ and remote sensing observations. We now apply the same procedure to the proton precipitation, using SI12 images.

4. Proton Energy Flux

[15] Since the SI12 images are only minimally contaminated by dayglow which may be efficiently removed, the method described above may be used to obtain statistical maps of the precipitating proton energy flux during both summer and winter. The maps derived for the summer and winter intervals employed here are shown in Figures 3a and 3b respectively, showing C-shaped morphologies during both seasons. The minimum is located in the morning sector near 1000–1100 MLT, while the maximum is observed in the midnight region. In summer the statistical maximum flux is 0.28 mW m^{-2} located in the postmidnight sector, while in winter the maximum is 0.24 mW m^{-2} located just before midnight. The magnitude of the proton energy flux is seen to be quite similar in summer and winter, while the latitudinal extent of the precipitation is greater in summer than in winter.

[16] For comparison, Figure 4 shows the Kp-weighted statistical proton energy flux patterns obtained from DMSP data by *Hardy et al.* [1989], using the method outlined above. Figures 4a and 4b show results for the summer and winter intervals, respectively, where we note that the difference arises solely from the different Kp values which occurred during the intervals and not from seasonal differences in the empirical model input. The C-shaped pattern is similar to that found here, with a minimum in the prenoon sector, and a maximum located in the 2300–2400 MLT sector reaching 0.35 mW m^{-2} for the summer interval and 0.24 mW m^{-2} for winter.

[17] To verify that our statistical results are not unduly influenced by the difference in the Kp values between the two seasons, we analyzed the seasonal variation in the proton energy flux separately for two ranges of Kp, namely $Kp \leq 3$ and $Kp \geq 4$. Results are summarized in Table 1. The energy fluxes were integrated over the complete auroral region (between 60° and 80° MLAT) for both ranges of Kp, and the ratio of the summer to the winter powers were evaluated. As can be seen in Table 1, the ratios are found to be 1.2 for both Kp ranges, indicating that overall, the area integrated proton energy flux in summer is ~20% larger than in winter. The seasonal difference thus exists independent of the Kp value. When all Kp values are taken together, the summer-winter total proton power ratio is found to be 1.5, this higher value being due to the distribution of samples with Kp in the two intervals. This value can also be obtained by weighting the averaged energy flux maps divided into the two Kp ranges for summer and winter (not shown) by the ratio between the number of cases in those Kp ranges and the total number of cases. Overall, the results for both ranges of Kp suggest that the difference in the magnetic activity during the two seasons is not the cause of the observed seasonal difference in the proton energy flux.

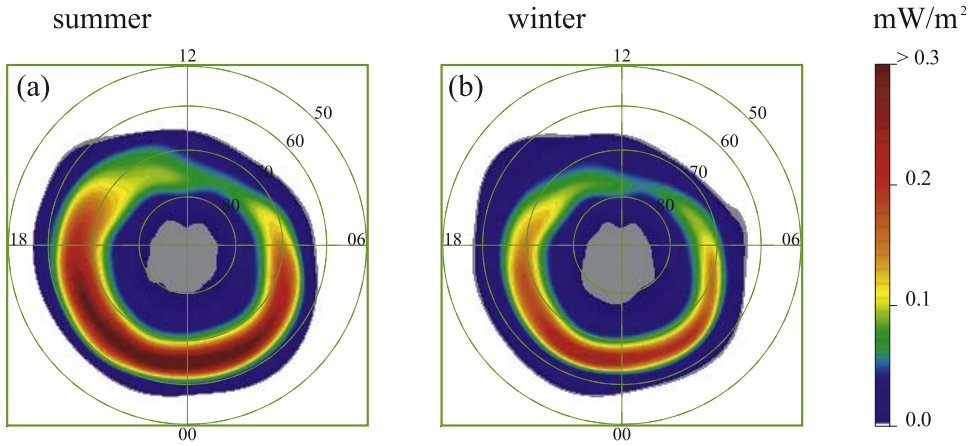

Figure 4. Proton energy flux from the *Hardy et al.* [1989] empirical model, using a Kp weighting evaluated for (a) our summer 2000 interval and (b) our winter 2000 interval.

[18] Observation of Figures 3a and 3b indicates that the seasonal difference in the proton energy flux comes mainly from the latitudinal extent of the precipitation. A confirmation of these findings was obtained through a parallel study consisting in studying the width of the proton oval observed by SI12 in two specific MLT sectors: 2200 ± 0.5 and 0200 ± 0.5 MLT. The poleward and the equatorward boundaries were defined by taking the 1/10th of the total count number of the emission peak in the sector considered. This study was made in both MLT sectors separately for November 2000 and June 2001. It shows that the equatorward boundary of the oval is globally located at lower latitude in summer than in winter, while the poleward boundary is located at higher latitude in summer than in winter. The average latitudinal width in June 2001 is 13.5° ± 2.9°, while it is 8.3° ± 1.9° in November 2000. These results, obtained over another time period, are in agreement with those described before. We also used boundaries determined from DMSP spectrograms [*Newell et al.*, 1996b] to verify whether the seasonal difference in the width of the proton oval is also present. The B5i boundary is defined as the poleward boundary of the auroral oval, determined by an abrupt drop in the ion energy flux, and B1i as the "zero-energy" ion boundary. We evaluated the latitudinal difference between those two boundaries and analyzed their seasonal variations. The DMSP oval crossings were selected in the 1630 and 2200 MLT sectors, where the proton oval is wider in summer according to our results. We first use the same time period as in this study, that is 12 days in summer 2000 and 15 days in winter 2000, corresponding to 181 and 317 DMSP oval crossings, respectively. The average latitudinal difference is 9.4° ± 3.0° in summer and 6.9° ± 1.5° in winter. In a second test, to extend the time period and confirm our results, we evaluated the averaged latitudinal difference between B5i and B1i over the months of June and July 2000 and over December 2000 and January 2001. The values are 8.8° ± 2.9° and 7.3° ± 1.6°, respectively. This result shows that the proton auroral oval is 19% wider in summer than in winter.

[19] To analyze the influence of the assumed proton energy on the seasonal effect, a test was made where the proton mean energy was set to 8 keV rather then using the statistical values from *Hardy et al.* [1989]. The 8-keV energy value is the mean energy of the midnight number flux maximum for a Kp value between 0 and 1 and is approximately half the value of the highest average energy of the entire auroral region in the same Kp range [*Hardy et al.*, 1989]. Results show that the morphology of the proton average energy flux pattern is very similar to Figures 3 for both seasons. The maximum in the proton energy flux is consistently located in the night sector and the minimum in the prenoon sector in winter and summer. The proton power, evaluated on the region between 60° and 80° MLAT, is ~3.2 GW in summer and ~1.7 GW in winter, while it was ~2.6 GW and ~1.7 GW, respectively, when using the *Hardy et al.*'s [1989] mean energy. The seasonal difference is still present with a higher ratio of 1.9 between the summer and winter powers. Since parallel electric fields that accelerate electrons downward and produce discrete arcs are weaker in summer than in winter, it is expected that protons would be more energetic during this season. We test the influence of an increase in the summer proton mean energy by evaluating the average energy flux pattern using a fixed energy of 15 keV and comparing with the calculation with the 8-keV energy. The 15-keV energy is the average energy characteristic of the midnight number flux maximum and around half the value of the average energy maximum for Kp ~ 3 [*Hardy et al.*, 1989]. The morphology of the high-latitude summer average energy flux is similar to the one showed in Figure 3a, with a maximum value of 0.43 mW m^{-2} and a total auroral

Table 1. Summary of the Characteristics of the Summer and Winter Samples for Two Ranges of Kp[a]

Kp	N_{summer}	N_{winter}	ϕ_{summer}	ϕ_{winter}
≤3	3526	5423	2.00	1.65
≥4	1400	253	4.32	3.73

[a]The first column gives the Kp range, while the second and third columns indicate the number of cases in each range over the summer and winter periods, respectively. The fourth and fifth columns then give (in GW) the proton power integrated over the whole auroral oval for both seasons.

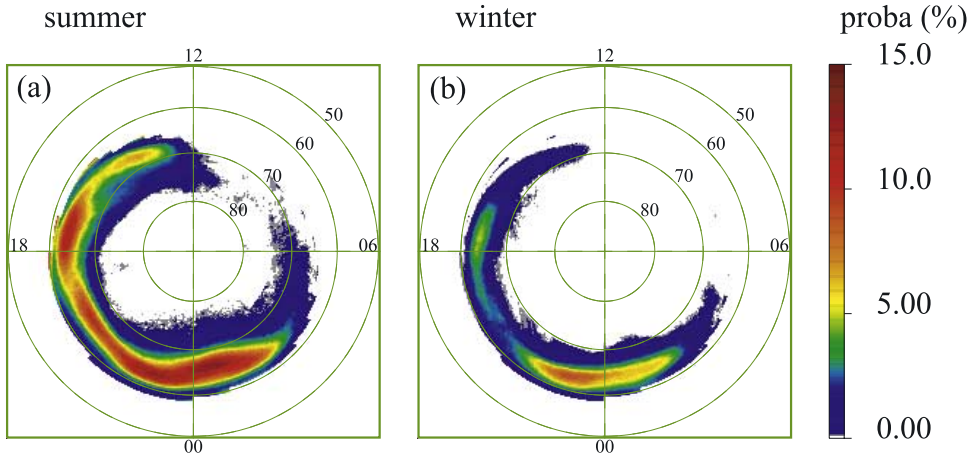

Figure 5. Probability of occurrence of intense proton aurora in (a) our summer and (b) our winter intervals, plotted in geomagnetic coordinates. An intense proton aurora is defined by a precipitating energy flux exceeding 0.5 mW m^{-2}.

power of 4.4 GW. The ratio between summer power with $\langle E_{pr} \rangle$ = 15 keV and winter power with $\langle E_{pr} \rangle$ = 8 keV is 2.6. This result shows that the seasonal difference is enhanced if the proton mean energy is also influenced by season. This trend may be expected since the Lyman-α efficiency function decreases with increasing proton mean energy [*Gérard et al.*, 2001]. The energy flux producing a given Lyman-α emission rate is consequently higher for higher proton energies.

[20] Comparing the winter energy fluxes for protons and electrons shown in Figures 3b and 1a, respectively, we find that the maximum proton energy flux is ~0.3 mW m^{-2} compared with 1.6 mW m^{-2} for electrons. The electron power over the uncontaminated sector between 60° and 80° MLAT is 19.4 GW and the proton power over the same region is 1.6 GW. Protons thus provide ~8% of the total precipitating particle energy flux. The C-shaped pattern for protons is roughly the mirror reflection in the noon-midnight meridian of the pattern for electrons. The minimum in electron flux is expected in the afternoon sector from Figure 1b, while for protons it is located in the morning sector, as previously noted by *Hardy et al.* [1989]. This feature can be explained by the grad-B and curvature drifts experienced by these particles. High-energy ions from the nightside plasma sheet drift preferentially westward via dusk into the afternoon and the late morning sectors and are thus excluded from much of the morningside oval [*Hardy et al.*, 1989]. On the other hand, the plasma sheet electrons drift eastward and are hence excluded from much of the afternoonside oval. The noon-midnight reflection symmetry between the electron and proton ovals is not perfect, however, since the maximum energy flux for both species is located in the same quadrant, around 2100 MLT for electrons and 2300 MLT for protons. This is the region where substorms are usually initiated, resulting in the direct injection of heated auroral plasma from the magnetotail. It can also be seen that in the dusk sector, the proton precipitation is located equatorward of the electron precipitation, as observed in previous studies [e.g., *Hardy et al.*, 1989; *Coumans et al.*, 2002]. Comparison of Figures 1a and 3b also shows that the winter electron oval is narrower than the proton oval in the sector between 1500 and 1800 MLT, while it is wider at later magnetic local times.

5. Probability of Intense Proton Aurora

[21] We next calculate the occurrence probability of intense proton aurora, defined by the occurrence of a proton energy flux higher than 0.5 mW m^{-2}. This value corresponds to 10% of the limit used for intense electron aurora, in approximate proportion to the fractional contribution of protons to the total particle energy flux. Results are shown in Figures 5a and 5b for our summer and winter intervals, respectively. The patterns again show a C-shaped morphology, with a minimum consistently in the morning sector between 0600 and 1200 MLT. The maximum probability in summer is located just after midnight with a value of ~15%, while in winter it is located just before midnight with a value of ~9%. When the probability distributions are integrated over the whole auroral region, the summer to winter ratio is found to be 2.9, implying that the global probability of occurrence of intense proton auroras is nearly 3 times higher in summer than in winter.

[22] We have also calculated the ratio of summer to winter mean probabilities in individual 1-hour sectors of MLT, shown (as inverse winter to summer ratios) in Figure 6. It can be seen that values are less than one in each sector, meaning that the probability of occurrence of intense proton events is higher in summer than in winter at all local times. Ratios are lower than 0.1 from 0500 to 1500 MLT and are essentially zero from 0800 to 1200 MLT, where no intense events were observed in winter. Ratios between 0.1 and 0.3 are observed from 1500 to 2100 MLT and from 0300 to 0500 MLT, while values are between 0.4 and 0.6 in the midnight sector from 2200 to 0200 MLT. We thus find that the probability is nearly twice as high in summer than in winter even in the sector where the winter probability is a maximum.

6. Discussion

[23] In this paper we have used IMAGE-FUV data to derive maps of the mean precipitating energy flux for

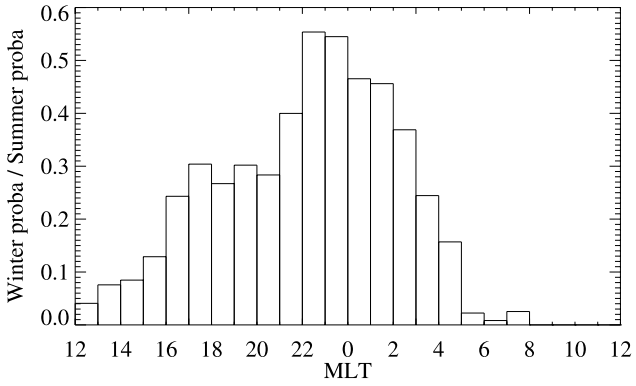

Figure 6. Histogram of the ratio between the integrated probabilities of occurrence of intense protons events in winter and summer evaluated for each 1-hour MLT sector. A ratio lower than 1, as observed, means that the probability is higher in summer than in winter. The average ratio for all MLT sectors is 0.35.

electrons in winter and for protons in both summer and winter. Our results for electrons show good agreement with previous results derived from in situ DMSP particle data and from Polar-UVI observations, both in morphology and in magnitude. For protons the agreement with previous results obtained from in situ DMSP data is very good. Thus we find that statistical maps based on DMSP overpass data that are not collected simultaneously at each MLT, and those from global images of the auroral region are in fact comparable. The results obtained here on auroral proton precipitation have then been compared with previous electron observations obtained from DMSP and Polar UVI data.

[24] Our proton results show that the total precipitating power integrated over the complete auroral oval is higher in summer than in winter. This is a consequence of the larger latitudinal extent of the proton oval in summer than in winter, while the peak value of the energy flux is quite similar for the two seasons. The occurrence probability of intense proton auroras, whose energy flux is higher than 0.5 mW m^{-2}, is also higher in summer than in winter, while intense electron precipitation is enhanced in the winter, as found in previous studies.

[25] In the following section we first discuss the origins of auroral protons and what acceleration process is associated with the intense events where the protons energy flux is higher than 0.5 mW m^{-2}. To address to this question, we have examined in situ particle measurements obtained by the ion and electron electrostatic analyzers on board the FAST spacecraft [*Carlson et al.*, 1998] during simultaneous crosses of such events observed by SI12. Protons producing emission observed by SI12 can either originate from the magnetospheric tail or from the ionosphere. Second, we consider several possible explanations for the seasonal difference emphasized in the proton precipitation: a seasonal variation in the geometry of the geomagnetic tail or seasonality in the modulation of electric fields accelerating protons downward into the atmosphere or retarding proton access to the atmosphere.

[26] The analysis of in situ particle measurements gives information about the energy spectra of proton during intense proton events. Instruments on board the FAST spacecraft [*Carlson et al.*, 1998] provide ion and electron energy-time spectrograms measured in the pitch angle range $0°-30°$ and pitch angle-time distributions for particles with energies higher than 1 keV. We selected cases where FUV observations showed a proton flux higher than 0.5 mW m^{-2} and simultaneous FAST measurements were available. Seven cases were found in winter 2000, when the FAST orbit was ideally located, crossing the auroral region in the 2200 MLT sector. The FAST data show that the intense proton aurora corresponds to precipitation of high-energy protons with energies above 1 keV, often up to at least 25 keV, which is the detector limit. The pitch-angle distribution of the precipitating ion during such events is isotropic. We also observed that as expected, the ion flux decreases during electron inverted-V events. The empirical proton precipitation model derived by *Hardy et al.* [1989] also shows that in the sector where intense proton aurora are more frequent, in the midnight sector around 63° MLAT, the mean proton energies lie between 5 and 30 keV for all Kp values.

[27] In a recent study, *Hultqvist* [2002] has analyzed Freja observations of downward nightside ion acceleration events at auroral latitudes, in ion spectra at energies up to 3.5 keV. He showed, among other things, that the ion pitch-angle distributions are generally somewhat field-aligned but not far from isotropic, that all ion species (H^+, O^+, and He^+) are accelerated to the same energy, and that such ion precipitation is generally not observed in regions with primary auroral Birkeland currents associated with electron inverted-V distributions. He concluded that a potential drop along the magnetic field lines can provide the observed kinetic energies and that the accelerated particles originated in the ionosphere. However, if such accelerated particles are limited to energies less than ~3 keV, this mechanism will produce only a small contribution in the overall proton energy flux. Moreover, the results of the comparison with the FAST spectrograms have shown that the intense proton events are usually due to precipitation of protons with higher energy. The ionospheric origin of the protons can thus be rejected.

[28] Possible mechanism of the observed seasonality may be due to variations in the geometry of the Earth magnetic environment. A seasonal variation of the magnetotail stretching may explain the seasonal variation in the proton precipitation. It has been shown that the main mechanism for proton precipitation is related to the nightside geometry of stretched magnetic field lines and its nonadiabatic effects on the ion motions [*Sergeev et al.*, 1983]. The auroral region can be subdivided into different zones whose boundaries may be determined from DMSP spectrograms [*Newell et al.*, 1996b]. The proton isotropy boundary described by *Sergeev et al.* [1983] is a good approximation to the earthward edge of the tail current sheet. In the DMSP automated classification, a proxy (b2i) for the ion isotropy boundary is defined as the precipitating energy flux maximum of high-energy (≥3 keV) ions [*Newell et al.*, 1996b]. Proton isotropy poleward of this boundary is a consequence of pitch angle scattering in the current sheet where the gyroradius is comparable to the magnetic field line curvature. The region located just poleward of the isotropy boundary is the main sector where intense proton aurora should occur. The level of stretching of magnetic field lines thus influences the degree to which ions are scattered. It is

well known that the magnetotail configuration depends on the dipole tilt toward and away from the Sun and is thus partly controlled by the seasons. However, ion scattering within the current sheet under any given conditions will produce the same isotropic population on both sides of the equatorial plane and hence the same "source" ion population on both "summer" and "winter" hemisphere field lines during solstice conditions. Therefore the magnetotail effects themselves will not produce a seasonal effect on the ion precipitation.

[29] Another possible mechanism explaining the seasonal variations of the proton precipitation is a variation in parallel electric fields. Downward electric field would increase the proton energy flux into the atmosphere and produce downward directed ion beams. This type of events has been observed in the auroral zone by the FAST satellite [*Klumpar et al.*, 2000]. Individual events are narrowly confined in latitude and display a latitude profile similar to electron inverted Vs. The acceleration process occurs at altitude above the FAST satellite (~4000 km) and is thought to be a quasistatic, downward directed, parallel potential structure. *Klumpar et al.* [2000] showed that these downward directed ion beams occur predominantly in the postmidnight sector, close to the region of the summer maxima in the proton energy flux and occurrence probability of intense proton aurora found in this work (Figures 3a and 5a). Such events may thus contribute to the intense events observed here in the summer data but would not be dominant as *Klumpar et al.*'s [2000] description of the spectral distribution does not agree with the results of the comparisons with FAST measurements described before. Peak characteristic energies of those downward directed ion beams often reach only 1 keV and the pitch angle distribution is not isotropic.

[30] Variations of the upward electric fields which downward accelerate auroral electrons, creating inverted-V events, and which would also influence the proton precipitation is also a possible cause of the seasonality of proton aurora. On the basis of measurements from the DMSP satellites, *Newell et al.* [1996a] has emphasized the suppression of discrete electron aurora in sunlit regions. As mentioned above, they interpreted the observations in terms of an ionospheric conductivity feedback mechanism [*Lysak*, 1986]. We suggest that this mechanism may also play an important role in the seasonal control of proton precipitation. In this picture the ionospheric "background conductance," the approximately constant ionospheric conductance due largely to solar ionization, plays a role in the formation of the aurora. A large-scale electric field is present in the ionosphere associated with magnetospheric plasma convection, which drives a large-scale system of electric current. The Pedersen component of these currents will close in the magnetosphere via large-scale field-aligned (Birkeland) currents. Precipitating particles create a density perturbation and thus increase the Pedersen conductivity. As mentioned in the introduction, the reaction of the ionosphere then depends upon its state. If the background conductivity is too high (i.e., on the dayside), the ionosphere responds by producing a polarization electric field that reduces the large-scale convection electric field and limit the current. If the background conductivity is low (i.e., on the nightside), the ionosphere responds with an increase in the Pedersen current, which must be closed by field-aligned currents flowing at the conductivity gradient. A larger current then flows between the magnetosphere and ionosphere, requiring a larger field-aligned potential drop to accelerate electrons downward from the low-density magnetosphere. A consequence of the positive feedback, which couples the enhanced current with the magnetosphere through field-aligned currents, is the formation of high-energy electron precipitation and intense electron auroral arcs. In addition to the downward acceleration of magnetospheric electrons, the field-aligned electric fields will also accelerate ionospheric ions upward into the magnetosphere, while downcoming magnetospheric ions will be decelerated. Observations of seasonal variations in the upward ion beams which correspond to the electron results of *Newell et al.* [1996a] were found by *Collin et al.* [1998] using data from the TIMAS instrument on board the Polar satellite [*Shelley et al.*, 1995]. FAST observations have also been used to study the upward directed ion beams accelerated by the field-aligned potential difference [*McFadden et al.*, 1999]. Since these field-aligned potentials will also suppress proton precipitation from the magnetosphere, less intense proton auroras may be expected in winter.

[31] We now quantitatively examine how proton and electron precipitation from the magnetosphere is affected by the presence of a field-aligned electric field. We use the kinetic theory due to *Knight* [1973], which has been employed in numerous studies of terrestrial auroral electron precipitation [e.g., *Lyons et al.*, 1979] and has been applied more recently to jovian conditions as well [e.g., *Cowley and Bunce*, 2001]. We consider the electrons first and assume that the magnetospheric plasma sheet "source" population is an isotropic Maxwellian of number density N and thermal energy $W_{th} = kT$. If these electrons are accelerated downward by an upward directed parallel electric field through a (positive) voltage $\varphi_{\|}$, their precipitating energy flux Q_0 ($\varphi_{\|}$) is

$$Q_0\left(\varphi_{\|}\right) = Q_0(0)\left[1 + \frac{e\varphi_{\|}}{W_{th}} + \frac{1}{2}\left(\frac{e\varphi_{\|}}{W_{th}}\right)^2\right],$$

where e is the electron charge and $Q_0(0)$ is the precipitating electron energy flux for zero field-aligned voltage, given by

$$Q_0(0) = 2NW_{th}\left(\frac{W_{th}}{2\pi m_e}\right)^{1/2}.$$

This expression for $Q_0(\varphi_{\|})$ was first derived by *Lundin and Sandahl* [1978]. It is based on two simple assumptions, the first being that the acceleration region is sufficiently compact along the field lines that no particles mirror before experiencing the full field-aligned potential. The second is that the acceleration region lies at a sufficient altitude that $(B_i/B_{\varphi_{\|}}) > (e\varphi_{\|}/W_{th})$, where B_i is the magnetic field strength in the ionosphere and $B_{\varphi_{\|}}$ is the field strength in the acceleration region. For the case of plasma sheet electrons decelerated by a downward directed electric field through a (negative) potential $\varphi_{\|}$, the expression becomes modified to

$$Q_0\left(\varphi_{\|}\right) = Q_0(0)\exp\left(\frac{e\varphi_{\|}}{W_{th}}\right).$$

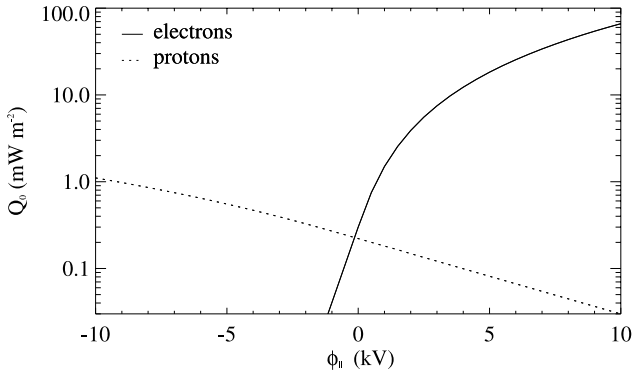

Figure 7. Variation of the precipitating electron and proton energy fluxes ($Q_0(\varphi_{||})$) with the field-aligned voltage ($\varphi_{||}$), for a plasma sheet "source" population with a number density of 0.5 cm^{-3} and proton and electron thermal energies (equal to kT) of 5 and 0.5 keV, respectively. A positive voltage implies an upward directed electric field. The solid line shows the electron energy flux, while the dashed line shows the proton energy flux.

With a change in the sign of the charge, similar expressions also apply to proton precipitation from the plasma sheet, where the upper expression for $Q_0(\varphi_{||})$ then becomes valid for negative voltages which accelerate protons downward into the ionosphere, while the lower expression is valid for positive voltages which decelerate the precipitating protons. Figure 7 then shows the variation of the electron (solid line) and proton (dashed line) energy fluxes as function of the field-aligned voltage $\varphi_{||}$, using realistic values for the plasma sheet number density and particle thermal energies. Specifically, we have used $N = 0.5$ cm^{-3} and $W_{th} = 0.5$ keV for electrons and 5 keV for protons [*Baumjohann et al.*, 1989]**.** It can be seen that for positive voltages corresponding to upward directed electric fields, the precipitating electron energy flux increases rapidly with the voltage, while the energy flux of the hotter magnetospheric protons more gradually declines. For example, if the potential difference doubles from 5 to 10 kV, then with these plasma sheet parameters the accelerated electron flux increases from 20 to 66 mW m^{-2}, while the proton energy flux decreases from 0.08 to less than 0.03 mW m^{-2}. For negative voltages corresponding to downward directed electric fields, however, the electrons are decelerated and the energy flux rapidly falls to very small values, while the proton energy flux steadily increases. It can thus be seen that if the above ionospheric conductivity feedback process seasonally modulates the electron-accelerating voltage as explained above, then a seasonal effect of the opposite sense will also occur in precipitating protons, as observed here.

[32] In view of the different points discussed above, the results of this study suggest that seasonal variation in proton precipitation probably originates mainly from seasonal variations in the field-aligned electric fields that accelerate particles from the magnetospheric tail, in each hemisphere, as a consequence of the variation of solar illumination.

[33] **Acknowledgments.** VC is supported by a fellowship from the Belgian Fund for Research in Industry and Agriculture (FRIA), JCG and BH are supported by the Belgian National Fund for Scientific Research (FNRS), and SWHC is supported by PPARC Senior Fellowship PPA/P/S/2002/00168. This work was funded by the PRODEX program of the European Space Agency (ESA) and the Belgian Fund for Collective and Fundamental Research (FRFC grant 2.4517.02). We acknowledge C.W. Carlson at U.C. Berkeley and CDAWeb for the FAST data.

[34] Arthur Richmond thanks David Evans and another reviewer for their assistance in evaluating this paper.

References

Baumjohann, W., G. Paschmann, and C. A. Cattell (1989), Average plasma properties in the central plasma sheet, *J. Geophys. Res.*, *94*, 6597.

Bisikalo, D. V., V. I. Shematovich, J.-C. Gérard, M. Meurant, S. B. Mende, and H. U. Frey (2003), Remote sensing of the proton aurora characteristics from IMAGE-FUV, *Ann. Geophys.*, *21*, 2165.

Carlson, C. W., R. F. Pfaff, and J. G. Watzin (1998), The Fast Auroral SnapshoT (FAST) mission, *Geophys. Res. Lett.*, *25*, 2013.

Collin, H. L., W. K. Peterson, O. W. Lennartsson, and J. F. Drake (1998), The seasonal variation of the auroral ion beams, *Geophys. Res. Lett.*, *25*, 4071.

Coumans, V., J.-C. Gérard, B. Hubert, and D. S. Evans (2002), Electron and proton excitation of the FUV aurora: simultaneous IMAGE and NOAA observations, *J. Geophys. Res.*, *107*(A11), 1347, doi:10.1029/2001JA009233.

Coumans, V., J.-C. Gérard, B. Hubert, M. Meurant, and S. B. Mende (2004), Global auroral conductance distribution due to electron and proton precipitation from IMAGE-FUV observations, *Ann. Geophys.*, *22*, 1595.

Cowley, S. W. H., and E. J. Bunce (2001), Origin of the main auroral oval in Jupiter's coupled magnetosphere-ionosphere system, *Planet. Space Sci.*, *49*, 1067.

Frank, L. A., and J. D. Craven (1988), Imaging results from Dynamics Explorer 1, *Rev. Geophys.*, *26*, 249.

Frey, H. U., S. B. Mende, C. W. Carlson, J.-C. Gérard, B. Hubert, J. Spann, R. Gladstone, and T. J. Immel (2001), The electron and proton aurora as seen by IMAGE-FUV and FAST, *Geophys. Res. Lett.*, *28*, 1135.

Gasda, S., and A. D. Richmond (1998), Longitudinal and interhemispheric variations of auroral ionospheric electrodynamics in a realistic geomagnetic field, *J. Geophys. Res.*, *103*, 4011.

Gérard, J.-C., B. Hubert, M. Meurant, V. I. Shematovich, D. V. Bisikalo, H. Frey, S. Mende, G. R. Gladstone, and C. W. Carlson (2001), Observation of the proton aurora with IMAGE FUV imager and simultaneous ion flux in situ measurements, *J. Geophys. Res.*, *106*, 28,939.

Hardy, D. A., M. S. Gussenhoven, and E. Holeman (1985), A statistical model of auroral electron precipitation, *J. Geophys. Res.*, *90*, 4229.

Hardy, D. A., M. S. Gussenhoven, and D. Brautigam (1989), A statistical model of auroral ion precipitation, *J. Geophys. Res.*, *94*, 370.

Hubert, B., J. C. Gérard, D. S. Evans, M. Meurant, S. B. Mende, H. U. Frey, and T. J. Immel (2002), Total electron and proton energy input during auroral substorms: Remote sensing with IMAGE-FUV, *J. Geophys. Res.*, *107*(A8), 1183, doi:10.1029/2001JA009229.

Hultqvist, B. (2002), Downward ion acceleration at auroral latitudes: Cause of parallel electric field, *Ann. Geophys.*, *20*, 1117.

Klumpar, D. M., M. Boehm, R. J. Strangeway, C. W. Carlson, J. P. McFadden, and M. A. Temerin (2000), Structured proton precipitation: A particle source for discrete proton aurora, *Eos Trans. AGU*, *81*(48), Fall Meet. Suppl., Abstract SM11C-11.

Knight, S. (1973), Parallel electric field, *Planet. Space Sci.*, *21*, 741.

Liou, K., P. T. Newell, and C.-I. Meng (2001), Seasonal effects on auroral particle acceleration and precipitation, *J. Geophys. Res.*, *106*, 5531.

Lummerzheim, D., M. Brittnacher, D. Evans, G. A. Germany, G. K. Parks, M. H. Rees, and J. F. Spann (1997), High time resolution study of the hemispheric power carried by energetic electrons into the ionosphere during the May 19/20, 1996 auroral activity, *Geophys. Res. Lett.*, *24*, 987.

Lundin, R., and I. Sandahl (1978), Some characteristics of the parallel electric field acceleration of electrons over discrete auroral arcs as observed from two rocket flights, in *Symposium on European Rocket Research, ESA SP-135*, p. 125, Eur. Space Agency, Noordwijk, Netherlands.

Lyons, L. R., D. S. Evans, and R. Lundin (1979), An observed relation between magnetic field aligned electric fields and downward electron energy fluxes in the vicinity of auroral forms, *J. Geophys. Res.*, *84*, 457.

Lysak, R. L. (1986), Coupling of the dynamic ionosphere to auroral flux tubes, *J. Geophys. Res.*, *91*, 7047.

McFadden, J. P., C. W. Carlson, and R. E. Ergun (1999), Microstructure of the auroral acceleration region as observed by FAST, *J. Geophys. Res.*, *104*, 14,453.

Mende, S. B., et al. (2000), Far ultraviolet imaging from the IMAGE spacecraft. 1. System design, *Space Sci. Rev.*, *91*, 243.

Mende, S. B., H. U. Frey, T. J. Immel, D. G. Mitchell, P. C:son-Brandt, and J.-C. Gérard (2002), Global comparison of magnetospheric ion fluxes and auroral precipitation during a substorm, *Geophys. Res. Lett.*, *29*(12), 1609, doi:10.1029/2001GL014143.

Meurant, M., J.-C. Gérard, B. Hubert, V. Coumans, V. I. Shematovich, D. V. Bisikalo, D. S. Evans, G. R. Gladstone, and S. B. Mende (2003), Characterization and dynamics of the auroral electron precipitation during substorms deduced from IMAGE-FUV, *J. Geophys. Res.*, *108*(A6), 1247, doi:10.1029/2002JA009685.

Newell, P. T., C.-I. Meng, and K. M. Lyons (1996a), Suppression of discrete aurorae by sunlight, *Nature*, *381*, 766.

Newell, P. T., Y. I. Feldstein, Y. I. Galperin, and C.-I. Meng (1996b), Morphology of nightside precipitation, *J. Geophys. Res.*, *101*, 10,737.

Newell, P. T., R. A. Greenwald, and J. M. Ruohoniemi (2001), The role of the ionosphere in aurora and space weather, *Rev. Geophys.*, *39*, 137.

Richmond, A. D. (1995), Ionospheric electrodynamics using magnetic apex coordinates, *J. Geomagn. Geoelectr.*, *47*, 191.

Sergeev, V. A., E. M. Sazhina, N. A. Tsyganenko, J. A. Lundblad, and F. Soraas (1983), Pitch-angle scattering of energetic protons in the magnetotail current sheet as the dominant source of their isotropic precipitation into the nightside ionosphere, *Planet. Space Sci.*, *31*, 1147.

Shelley, E. G., et al. (1995), The Toroidal Imaging Mass-Angle Spectrograph (TIMAS) for the POLAR mission, *Space Sci. Rev.*, *71*, 497.

Vallance Jones, A., F. Creutzberg, R. L. Gattinger, and F. R. Harris (1982), Auroral studies with a chain of meridian-scanning photometers: 1. Observation of proton and electron aurora in magnetospheric substorms, *J. Geophys. Res.*, *87*, 4489.

V. Coumans, J.-C. Gérard, and B. Hubert, Institut d'Astrophysique et de Géophysique (B5c), Université de Liège, Allée du 6 août, 17, 4000, Liège, Belgium. (v.coumans@ulg.ac.be; jc.gerard@ulg.ac.be; b.hubert@ulg.ac.be)

S. W. H. Cowley, Department of Physics and Astronomy, University of Leicester, Leicester, LE1 7RH, UK. (swhcl@ion.le.ac.uk)

S. B. Mende, Space Sciences Laboratory, University of California, Berkeley, CA 94720-7450, USA. (mende@ssl.berkeley.edu)